

Research Article

Open Access



# Effects of processing parameters on a $\beta$ -solidifying TiAl alloy fabricated by laser-based additive manufacturing

Danni Huang<sup>1,2</sup>, Yangping Dong<sup>2</sup>, Hancong Chen<sup>2</sup>, Yinghao Zhou<sup>2</sup>, Ming-Xing Zhang<sup>1</sup>, Ming Yan<sup>2</sup>

<sup>1</sup>School of Mechanical and Mining Engineering, The University of Queensland, Queensland 4072, Australia.

<sup>2</sup>Department of Materials Science and Engineering and Shenzhen Key Laboratory for Additive Manufacturing of High-Performance Materials, Southern University of Science and Technology, Shenzhen 518055, Guangdong, China.

**Correspondence to:** Prof. Ming-Xing Zhang, School of Mechanical and Mining Engineering, The University of Queensland, St. Lucia, Queensland 4072, Australia. E-mail: mingxing.zhang@uq.edu.au; Prof. Ming Yan, Department of Materials Science and Engineering and Shenzhen Key Laboratory for Additive Manufacturing of High-Performance Materials, Southern University of Science and Technology, 1088 Xueyuan Blvd, Nanshan, Shenzhen 518055, Guangdong, China. E-mail: yanm@sustech.edu.cn

**How to cite this article:** Huang D, Dong Y, Chen H, Zhou Y, Zhang MX, Yan M. Effects of processing parameters on a  $\beta$ -solidifying TiAl alloy fabricated by laser-based additive manufacturing. *Microstructures* 2022;2:2022019. <https://dx.doi.org/10.20517/microstructures.2022.17>

**Received:** 30 Jul 2022 **First Decision:** 31 Aug 2022 **Revised:** 13 Sep 2022 **Accepted:** 22 Sep 2022 **Published:** 28 Sep 2022

**Academic Editor:** Ting Zhu **Copy Editor:** Fangling Lan **Production Editor:** Fangling Lan

## Abstract

$\beta$ -solidifying TiAl alloys are considered as promising candidate materials for high-temperature structural applications. Laser-based additive manufacturing (LAM) enables the fabrication of components with geometrical complexity in near-net shape, leading to time and feedstock savings. In this study, a gas-atomized Ti-44Al-4Nb-1Mo-1Cr powder is used as a feedstock material for LAM. However, the LAM of TiAl alloys remains a challenge due to serious cracking during the printing process. To minimize the cracking, the optimization of the LAM processing parameters is essential. Hence, the effects of the LAM processing parameters on the cracking susceptibility and microstructure are studied here. Our experimental results show that the cracking susceptibility can be mitigated by increasing the laser power. Accordingly, the microstructure transforms from the dominating  $\alpha_2$  grains to a near-lamellar microstructure with an increment in laser power, leading to a reduction in microhardness, even though it is still higher than that of its as-cast counterparts. It is concluded that changes in the laser power can directly tailor the microstructure, phase composition and microhardness of LAM-fabricated TiAl alloys.



© The Author(s) 2022. **Open Access** This article is licensed under a Creative Commons Attribution 4.0 International License (<https://creativecommons.org/licenses/by/4.0/>), which permits unrestricted use, sharing, adaptation, distribution and reproduction in any medium or format, for any purpose, even commercially, as long as you give appropriate credit to the original author(s) and the source, provide a link to the Creative Commons license, and indicate if changes were made.



**Keywords:**  $\beta$ -solidifying TiAl alloy, laser-based additive manufacturing, phase, microstructural evolution, microhardness

## INTRODUCTION

Intermetallic TiAl alloys are considered as excellent candidates for replacing Ni- and Ti-based alloys in aerospace applications due to their attractive properties, including low densities (3.8-4.2 g/cm<sup>3</sup>), which are around half those of Ni-based alloys (8-9 g/cm<sup>3</sup>)<sup>[1]</sup>, high specific strength and creep resistance at elevated temperatures and better oxidation resistance than conventional Ti alloys, particularly at 600-800 °C<sup>[2,3]</sup>. After several years of fundamental research, novel  $\beta$ -solidifying TiAl alloys have been developed, which offer opportunities for weight reduction and an operating temperature of increase up to 850 °C<sup>[4,5]</sup>. These TiAl alloys are characterized by a high content of  $\beta$ -stabilizing elements, such as Nb and Mo, and composed of complex multi-phases<sup>[5]</sup>, including the existence of a high volume fraction of  $\beta$  phase or its ordered counterparts,  $\beta_0$ <sup>[6]</sup>.

In contrast to conventional TiAl alloys, which solidify via a peritectic solidification path (i.e.,  $L \rightarrow L + \beta \rightarrow \alpha \rightarrow \dots$ ), resulting in significant texture and segregation,  $\beta$ -solidifying TiAl alloys solidify via the  $\beta$  phase (i.e.,  $L \rightarrow L + \beta \rightarrow \beta \rightarrow \dots$ ), showing an isotropic microstructure with modest segregation<sup>[7]</sup>. The principal constituents in  $\beta$ -solidifying TiAl alloys at room temperature are  $\gamma$ -TiAl (an ordered face-centered tetragonal  $L1_0$  structure,  $P4/mmm$ ,  $a = 0.3997$  nm and  $c = 0.4062$  nm),  $\alpha_2$ -Ti<sub>3</sub>Al (an ordered hexagonal  $D0_{19}$  structure,  $P6_3/mmc$ ,  $a = 0.5765$  nm and  $c = 0.46833$  nm) and  $\beta_0$  (an ordered body-centered  $B2$  structure,  $Pm\bar{3}m$ )<sup>[8]</sup>. However, due to the development of a long-range ordering of intermetallics, TiAl alloys exhibit intrinsic brittleness, meaning their development has been further impeded by a lack of design practice and processing difficulties<sup>[9]</sup>. A conventional casting process has been established for the mass production of TiAl components, but this is time-consuming, and its coarse as-cast microstructure is prone to causing microstructural inhomogeneity and poor room-temperature mechanical properties<sup>[10]</sup>.

Additive manufacturing (AM) enables the fabrication of near-net-shape components with complex geometries at higher efficiency and lower costs, compared with conventional manufacturing technologies<sup>[11,12]</sup>. Thus, AM has significant potential for manufacturing TiAl alloys and is of technical and economic interest. So far, several works have demonstrated that electron beam melting (EBM) is capable of directly making TiAl near-net-shape parts<sup>[13-15]</sup>. However, significant Al loss and inhomogeneous microstructures were found in TiAl alloys produced from EBM<sup>[16,17]</sup>, which are inevitably detrimental to the mechanical properties of the alloys. Compared to EBM, laser-based additive manufacturing (LAM) exhibits superior dimensional and surface finish qualities and lower machine costs due to the use of a finer laser beam and feedstock powder<sup>[18]</sup>. However, the major problem encountered during LAM is cracking<sup>[19]</sup>. In LAM, the high energy input and small heat-affected zone result in a high cooling rate ( $10^4$ - $10^6$  K/s) and the generation of high thermal stress<sup>[20]</sup>, which brittle TiAl alloys cannot accommodate, leading to cracking and distortion. Due to the nature of the additive layers, the LAM process experiences a complex thermal history involving melting, subsequent solidification and numerous lower temperature reheating cycles, which lead to very specific microstructures<sup>[21]</sup>. Most published works have shown that the adjustment of processing parameters can alleviate the internal defects and tailor the microstructure<sup>[22,23]</sup>, since the properties of TiAl alloys are strongly dependent on the microstructure<sup>[24-26]</sup>.

To incorporate advanced manufacturing technology using novel materials, knowledge of processing-related properties is of great importance. Thus, in this study, the microstructural characterization of a  $\beta$ -solidifying TiAl alloy fabricated by LAM with different laser powers is presented. The influence of laser power on the

internal defects, microstructural features and microhardness are evaluated to better understand the effects of processing parameters on the LAM-based  $\beta$ -solidifying TiAl alloy.

## EXPERIMENTAL PROCEDURE

The  $\beta$ -solidifying TiAl alloy with nominal composition Ti-44Al-4Nb-1Mo-1Cr (at.%) was used as the feedstock for LAM in the present study. The pre-alloyed spherical powder with particle sizes ranging from 47.8 to 130.0  $\mu\text{m}$  was supplied by Xi'an Sailong Metal Materials Co., Ltd. The powder morphology is depicted in [Figure 1A](#). Prior to printing, the powder was dried at 80 °C for 2 h under a vacuum to remove moisture.

An Optomec LENS 450 machine was used to print the TiAl alloy samples on Ti-6Al-4V substrates. The laser power was altered while other parameters were kept constant, as listed in [Table 1](#). Basically, the LENS 450 machine uses a 1064 nm wavelength Nd:YAG laser, a four-nozzle coaxial powder feeder, a controlled environment chamber and a motion control system. During the printing process, a high-powered laser beam is focused onto the substrate while the alloy powders are injected into the substrate from the powder delivery nozzles<sup>[27]</sup>. Upon interaction with the energy source, the powder was melted almost instantly, creating melt pools and then solidifying rapidly as the energy source moved away<sup>[11]</sup>. Successive layers are sequentially deposited to build the designed geometry. The printing process was conducted in an Ar-purged processing chamber where an oxygen content of less than 10 ppm was maintained to avoid oxidation. The cubic parts (10 mm  $\times$  10 mm  $\times$  10 mm) were built for further metallographic characterization. The printing scheme used in this study was a bi-directional scan in the X-Y plane without rotation between the layers.

The as-printed samples were sectioned along the longitudinal planes, which were parallel to the building direction, followed by mechanically grinding and polishing and chemically etching with Keller's reagent (4 vol.% HNO<sub>3</sub>, 2 vol.% HF and 94 vol.% H<sub>2</sub>O) to reveal the general structure<sup>[28]</sup>. An optical microscope (Zeiss Axio Observer 3) was used to investigate the defects. The microstructures of the pre-alloyed powder and as-printed samples were characterized by a Zeiss Merlin field-emission scanning electron microscope (SEM). The grain morphologies of the as-printed samples were observed using electron backscattered diffraction (EBSD, Zeiss Merlin, operated at 20 kV and 5 nA). The phase identification of the as-printed samples was performed with X-ray diffraction (XRD, Bruker D8) using Cu K $\alpha$  radiation. The diffraction angle ranged from 20° to 100° with a step size of 0.01°. XRD analysis was carried out on the longitudinal planes of the alloys produced from LAM. The binary phase diagram of the Ti-Al system provides effective guidance for studying the phase transformation process. The binary Ti-Al phase diagram was calculated with the aid of Thermo-Calc software on the basis of a commercially available thermodynamic database.

The Vickers microhardness was measured on a microhardness tester (HXD-1000TMC, Shanghai Taiming Optical Instrument Corporation, China) with a 300 g load held for 15 s. At least ten measurements were taken for each sample.

## RESULTS AND DISCUSSION

### LAM-based $\beta$ -solidifying TiAl alloy

The scanning electron microscope-energy dispersive X-ray spectroscopy (SEM-EDS) measured elemental concentrations of the pre-alloyed powder and the as-printed samples fabricated with different laser power inputs are listed in [Table 2](#). Negligible changes in the chemical composition of the as-printed alloys after LAM were detected in comparison to the original pre-alloyed powder. Hence, the chemical composition of the as-printed samples was not affected by the LAM process in this study.

**Table 1. Design of LAM processing parameters for  $\beta$ -solidifying TiAl alloy**

Parameters	Value
Laser power (W)	230, 260, 290, 320, 350 and 380
Laser scan speed (mm/min)	650
Powder feeder rate (rpm)	4
Layer thickness (inches)	0.01
Hatching spacing (inches)	0.015
Argon	99.999% purity

LAM: Laser-based additive manufacturing.

**Table 2. EDS analysis results showing elemental concentrations for pre-alloyed powder used and as-printed samples**

Sample	Ti (wt.%)	Al (wt.%)	Nb (wt.%)	Mo (wt.%)	Cr (wt.%)
Powder	58.18	29.93	8.23	2.33	1.35
230 W	59.23	30.11	7.69	1.61	1.37
260 W	57.32	31.79	7.91	1.67	1.32
290 W	58.21	30.96	7.77	1.79	1.29
320 W	58.15	30.90	7.89	1.73	1.34
350 W	57.94	31.02	8.02	1.71	1.31
380 W	58.09	31.21	7.65	1.61	1.34

EDA: Energy dispersive X-ray spectroscopy.

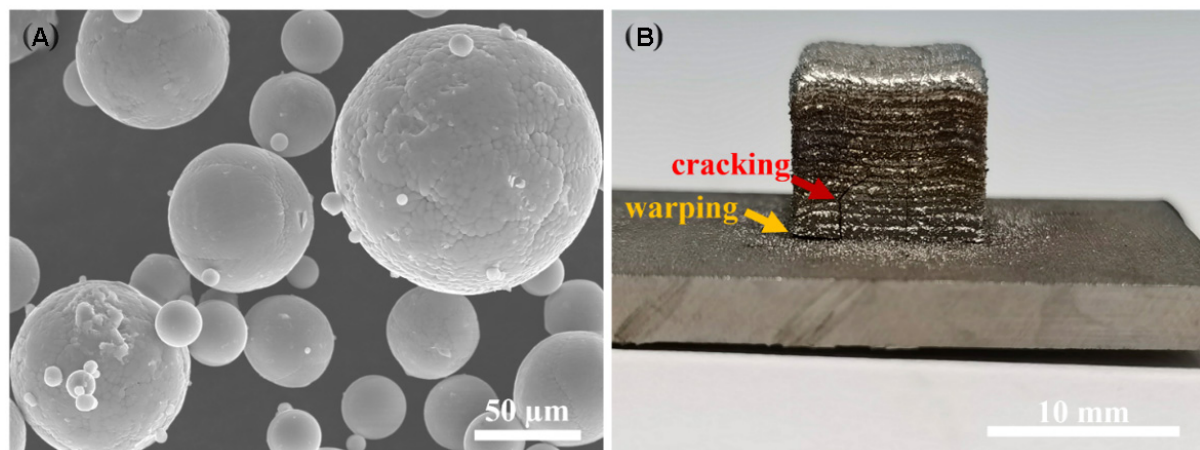


**Figure 1.** (A) Pre-alloyed Ti-44Al-4Nb-1Mo-1Cr powder morphology. (B) Representative image showing macrographs of as-printed specimens built with a laser power of 320 W.

The typical appearance of the LAM-fabricated  $\beta$ -solidifying TiAl samples with dimensions of 10 mm  $\times$  10 mm  $\times$  10 mm is shown in [Figure 1B](#). The surface of the as-printed sample is metallic and shiny, which implies that oxidation is negligible during the printing processing. However, visual observation of as-printed sample shows that the samples contain obvious surface defects, cracks and warping. Those are common defects encountered in additive manufacturing. During the printing process, the material experiences a large thermal gradient, leading to residual thermal stresses. The brittle TiAl alloy is unable to tolerate such high stresses, resulting in cracking and warping. Moreover, warping usually starts from the corner. With each newly deposited layer, the residual stresses accumulate, finally resulting in the part peeling away from the substrate<sup>[29]</sup>. The separation of the printed sample from the substrate is emphasized

by the orange arrow in Figure 1B. The most critical issue is the occurrence of cracking associated with the LAM of the TiAl alloy, which usually originates from the edge of the sample and at the interface between the sample and substrate. This observation agrees with previous studies of the LAM of TiAl alloys<sup>[19,30]</sup>.

The relationship between cracking susceptibility and laser power was further investigated. All as-printed samples produced with different laser powers contain cracks, as indicated by the red arrows in Figure 2. At a very low laser power of 230 W, the long and deep cracks originated from the edge of the sample and propagated along the building direction of the as-printed sample, as shown in Figure 2A. However, increasing the laser from 230 to 380 W led to alleviation of the cracking in the as-printed samples, as shown in Figure 2B-F. Only short cracks were observed as the laser increased to 380 W [Figure 2F]. The cracking in LAM is ascribed to the generation of thermal stress, which is caused by a large thermal gradient during laser heating. The extent of cracking is expected to be severe because brittle TiAl alloys cannot accommodate such high stress through deformation. The energy density input is defined as the energy per unit area, which is calculated by<sup>[30]</sup>:

$$E = \frac{P}{vD} \quad (1)$$

where  $P$  is the laser power,  $v$  is the scanning speed and  $D$  is the laser beam diameter. The cooling rate during the printing process is dependent on the energy input based on Rosenthal's three-dimensional solution<sup>[31]</sup>, which can be expressed as follows:

$$\frac{\partial T}{\partial t} \propto \frac{k(T-T_0)^2}{P/v} \quad (2)$$

where  $k$  is the thermal conductivity of the material and  $T_0$  is the substrate temperature. The cooling rate is inversely proportional to the energy density. A higher energy density can increase the width of the melt pool's contact with the substrate, thereby producing a larger melt pool that can maintain fluidity for a long period and prevent a high cooling rate<sup>[25]</sup>. Therefore, the mitigation of the cracking is attributed to the lower cooling rate resulting from the higher energy input.

### Microstructure and phase analysis

XRD was used to determine the phase constituents of the LAM-based samples fabricated with different laser powers. To better understand the phase transformation during the solidification process, a calculated Ti-Al phase diagram is provided in Figure 3B. The XRD patterns obtained across the building direction confirm the existence of three phases. The results, as presented in Figure 3A, reveal that the diffraction peaks belong to the  $\alpha_2$ ,  $\gamma$  and  $\beta_0$  phases in the as-printed samples. There is a slight deviation at a few peaks, which is ascribed to the change in the size of the tested specimens and the lattice imperfection caused by the high cooling rate and complex thermal history during the LAM process. It is noteworthy that more diffraction peaks of the  $\gamma$  phase could be detected with increasing laser power. This result illustrates that the content of the  $\gamma$  phase gradually increases with enhanced laser power.

The general microstructure appears to be refined in comparison to the conventionally processed TiAl alloys<sup>[4]</sup> due to the higher cooling rate. Different microstructures could be observed for the as-printed alloys depending on the laser power. The microstructures of the as-printed TiAl alloys manufactured with low laser power consist of mostly  $\alpha_2$  phases [Figure 4A and B], which are not typical for TiAl alloys. These are related to the high cooling rates, which suppress the formation of lamellar, because the diffusion-controlled

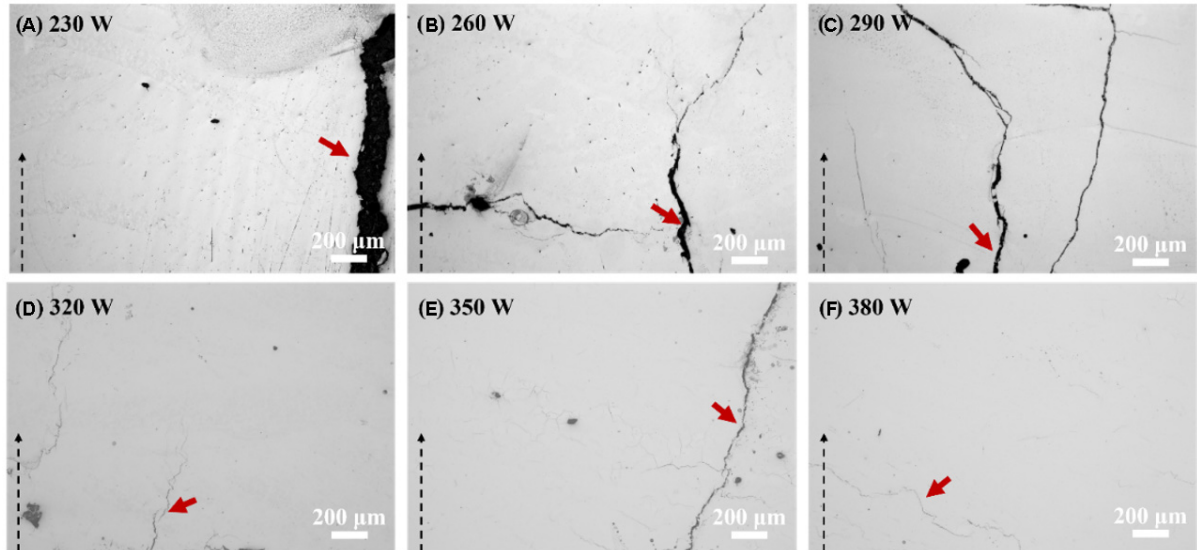


**Figure 2.** Cross-section views of as-printed samples with different laser powers: (A) 230; (B) 260; (C) 290; (D) 320; (E) 350; (F) 380 W. Internal defects are observed on the ground and polished samples. Dashed arrows indicate the build direction.

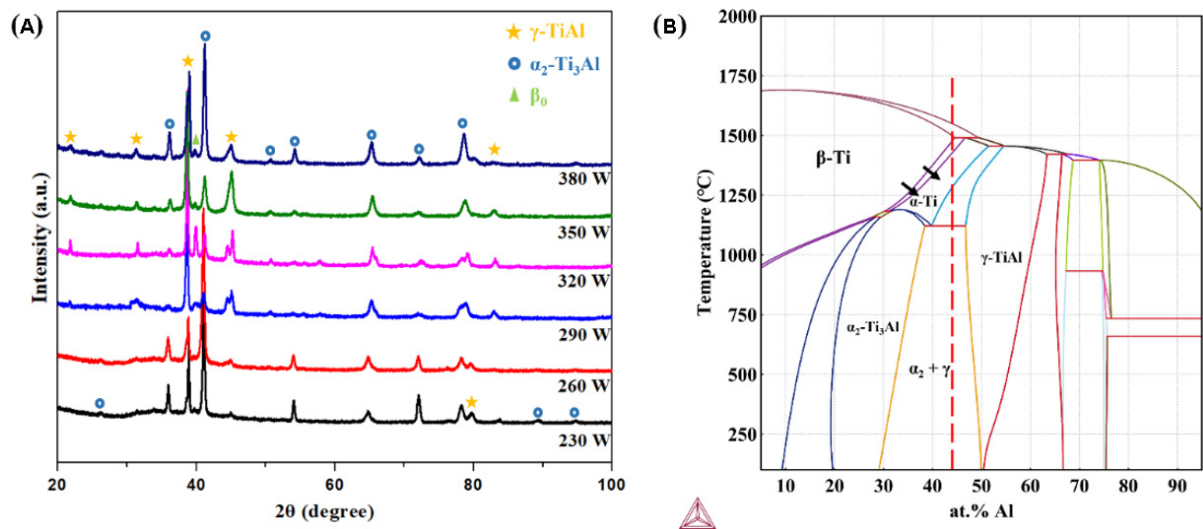


**Figure 3.** (A) XRD patterns of as-printed samples fabricated by different laser powers of 230, 260, 290, 320, 350 and 380 W. (B) Phase diagram for Ti-Al alloy (at.%). The arrows indicate the movement of the phase boundaries for  $\beta$ -stabilizing element additions. XRD: X-ray diffraction.

phase transformation of  $\alpha \rightarrow \alpha_2 + \gamma$  is sensitive to the cooling rate<sup>[32]</sup>. For the as-printed specimens fabricated using laser powers of 230 and 260 W, the cooling rate is high enough that the  $\alpha \rightarrow \alpha_2$  transformation took place. The lamellar colonies could be recognized in some regions with the intermediate laser power of 290 W [Figure 4C]. A very fine irregular near-lamellar structure formed as the laser power increased to 320 W.

The equiaxed  $\gamma$  (dark) grains and  $\beta_0$  (bright) phase decorate the  $\alpha_2/\gamma$  colony boundaries, as indicated by the green and blue arrows, respectively, in Figure 4D. Since the strong  $\beta$ -stabilizing elements of Nb and Mo concentrated in the primary  $\beta$  phase at high temperature and were hard to diffuse during a shorter time, the

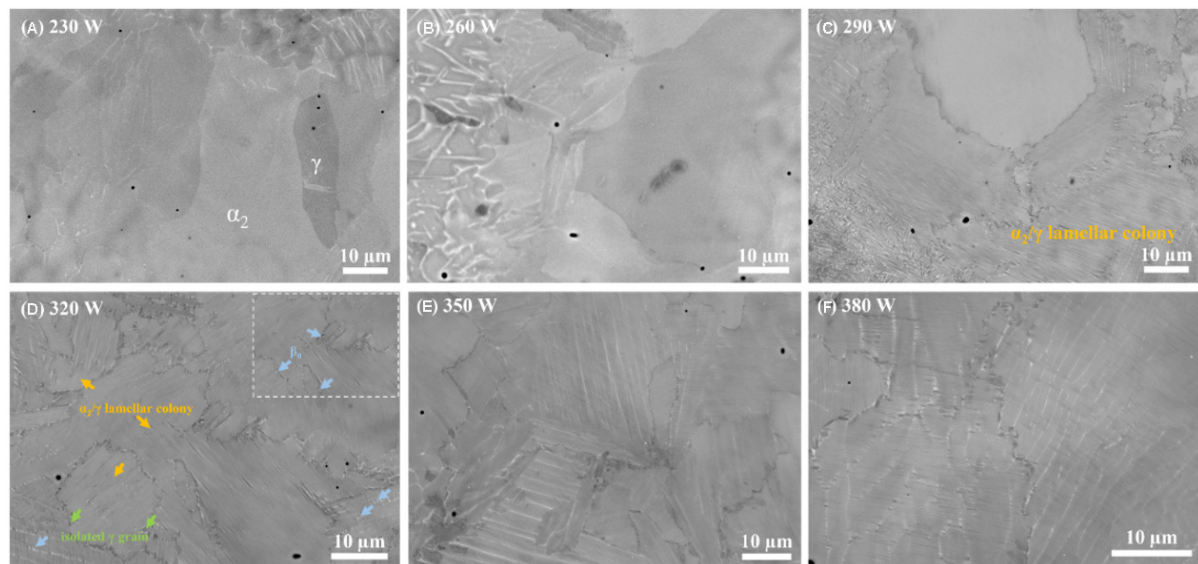


**Figure 4.** SEM-BSE images showing the effect of laser power on microstructures of LAM-based TiAl alloys: (A) 230; (B) 260; (C) 290; (D) 320; (E) 350; (F) 380 W. The insert shows the details at higher magnification. SEM: Scanning electron microscope.

primary  $\beta$  phase could not completely decompose into the  $\alpha$  phase. Part of the primary  $\beta$  phase would be retained and directly ordered to the  $\beta_0$  phase upon the further cooling process, which was distributed along the grain boundary, as indicated in Figure 4D. Moreover, it can be found that the  $\beta_0$  phase can be identified within the lamellar colonies, which is consistent with the previous works of Xu *et al.*<sup>[33]</sup> and Schwaighofer *et al.*<sup>[34]</sup>. They demonstrated that the  $\beta_0$  phase formed from the reaction  $\alpha \rightarrow \beta + \gamma$ , which also confirmed the existence of the  $(\beta + \alpha + \gamma)$  phase field and no single  $\alpha$  phase region was observed in the currently studied alloy. When further increasing the laser power, no obvious morphology change was observed, as depicted in Figure 4E and F.

To understand the formation of the microstructure, the Ti-Al binary phase diagram is provided, as shown in Figure 3B, which is calculated by the Thermo-Calc analysis. However, in the case of the  $\beta$ -solidifying TiAl alloy, due to the existence of  $\beta$ -stabilizing elements, Nb, Mo and Cr in this study shift the single  $\beta$ -Ti phase boundaries to a higher Al content regime, thus expanding the  $\beta$ -Ti phase field, as indicated by the black arrow in Figure 3B. Since the  $\beta$ -solidifying TiAl alloy contains sufficient  $\beta$ -stabilizing elements, the solidification pathway would be more complicated than the conventional casting of the TiAl alloy<sup>[33]</sup>. Therefore, the solidification pathway in our study takes place completely via the  $\beta$  phase following the sequence:  $L \rightarrow L + \beta \rightarrow \beta \rightarrow \beta + \alpha \rightarrow \beta + \alpha + \gamma \rightarrow \beta + \alpha_2 + \gamma \rightarrow \beta_0 + \alpha_2/\gamma + \gamma$ . The  $\alpha_2$  and  $\beta_0$  phases are ordered  $\alpha$  and  $\beta$  phases, respectively, at low temperatures<sup>[35]</sup>. After solidification and upon further cooling, the disordered hexagonal  $\alpha$  nucleates following the Burgers orientation relationship as  $(0001)_\alpha \parallel \{110\}_\beta$  and  $\langle 11\bar{2}0 \rangle_\alpha \parallel \langle 1\bar{1}1 \rangle_\beta$ <sup>[36]</sup>. Upon continuous cooling, the  $\alpha$  phases transform to either  $\alpha_2$ ,  $\gamma$  or a mixture of both, depending on the cooling rate<sup>[37]</sup>. The  $\alpha \rightarrow \alpha_2 + \gamma$  solid-state transformation is sensitive to the cooling rate<sup>[38]</sup>. The formation of  $\gamma$  lath in the  $\alpha$  phase is controlled by the long-range diffusion process<sup>[39]</sup>. At a lower cooling rate, the  $\gamma/\alpha_2$  lamellar structure could be observed in some regions, which resulted from precipitation of  $\gamma$  lamellae in the  $\alpha$  matrix, obeying the Blackburn orientation relationship. At the higher cooling rate, the high-temperature  $\alpha$  phase is only ordered into  $\alpha_2$  instead of decomposing to the  $\gamma$  phase<sup>[24,40]</sup>. The brittle  $\alpha_2$  phases, which are unable to withstand the deformation, are supposed to be responsible for the cracking.

The lamellar colony consists of  $\alpha_2$ -Ti<sub>3</sub>Al and  $\gamma$ -TiAl, which stems from the solid-state phase transformation. The ultrafine and closely packed lamellae, which are alternating  $\alpha_2$ -Ti<sub>3</sub>Al and  $\gamma$ -TiAl, are further characterized by TEM in detail, as shown in Figure 5. According to the TEM bright-field images in Figure 5A, fine lamellar with an average lamellar spacing on a nanoscale (44 nm) is presented, while the lamellar spacing is 1-2  $\mu\text{m}$  in the case of conventionally processed TiAl alloys<sup>[41]</sup>. The insert selected area electron diffraction proved the Blackburn orientation relationship between the  $\alpha_2/\gamma$  lamellae, which is  $(111)_\gamma \parallel [(0001)_{\alpha_2} \text{ and } \langle 110 \rangle_\gamma] \parallel \langle 11 \bar{2}0 \rangle_{\alpha_2}$ <sup>[42]</sup>. Several studies found that fined-grained lamellar colonies with few soft  $\gamma$  grains at the colony boundaries performed good creep strength, high fracture toughness and adequate ductility for as-cast TiAl alloys<sup>[43,44]</sup>.

### Grain features

EBSDBSD was introduced and conducted on the representative LAM-based TiAl alloy samples fabricated by different laser powers of 230, 290 and 350 W to characterize the influence of laser power on grain features, which are relevant to the energy density inputs<sup>[24,45]</sup>. The EBSD phase map of the as-printed TiAl alloy fabricated at 230 W, as shown in Figure 6A, demonstrates that the microstructure is dominated by the  $\alpha_2$  phase (green) and a small amount of  $\gamma$  (red) and  $\beta_0$  (yellow). The content of the  $\gamma$  phase increases with the reduction of the  $\alpha_2$  phase with increasing laser power. This phenomenon is ascribed to the competition between  $\alpha \rightarrow \alpha + \gamma \rightarrow \alpha_2 + \gamma$  transformation and the direct-ordering  $\alpha \rightarrow \alpha_2$  reaction<sup>[46]</sup>. According to Equation (2), a lower laser power resulted in a higher cooling rate, in which case the growth of  $\gamma$  lamellae was suppressed because of a shorter time for passing through the  $(\alpha + \gamma)$  phase region. The direct-ordering  $\alpha \rightarrow \alpha_2$  reaction was more favored under faster cooling conditions. Therefore, the microstructure built with a lower laser power was dominated by the  $\alpha_2$  phase. The microstructure was then dominated by the  $\gamma$  phase as the laser power increased to 290 W [Figure 6B]. The EBSD results are in good agreement with the XRD patterns. The detected  $\beta_0$  phase is mainly distributed along the grain boundary. It should be noted that the  $\beta_0$  phase located within lamellar colonies is on the nanoscale and the  $\alpha_2$  lamellae are extremely thin ( $\sim 10$  nm). Thus, some  $\alpha_2$  and  $\beta_0$  phases in Figure 6C are underdetected due to the resolution limit of EBSD.

EBSDBSD inverse pole figure maps are presented for each specimen in Figure 7A-C. The different colors correspond to different orientations in grains with respect to the crystal lattice. A multi-orientation of grains is distributed along the building direction. To measure the grain size, the representative band contrast maps, which provide higher contrast for counting, are shown in Figure 7D-F. Moreover, the average grain sizes of the as-presented samples were calculated to be 10.68, 14.50 and 25.77  $\mu\text{m}$ , respectively. The grain size increases with increasing laser power. Figure 8 presents the grain misorientation angle map. The grain boundaries were categorized as low-angle grain boundaries ( $< 15^\circ$ , LAGBs) and high-angle grain boundaries ( $> 15^\circ$ , HAGBs). Obviously, the as-printed alloys are dominated by HAGBs with percentages of 92.12%, 97.68% and 98.54%, respectively. HAGBs are generally caused by dynamic recrystallization<sup>[4]</sup>. Because LAM is a layer-wise addition process, this process involves several reheating cycles due to successive laser track and laser deposition. The previously solidified layers would be inevitably reheated when making a new layer. This phenomenon is similar to the annealing heat treatment in which recrystallization would take place<sup>[47]</sup>. Furthermore, the content of HAGBs is observed to increase with increasing laser power. An increase in laser power will result in a lower solidification rate and provide a longer time for remelting and recrystallization. Therefore, the grain features could be tailored by varying the applied laser power.

### Microhardness

To investigate the role of the processing parameters in determining the mechanical properties, microhardness measurements were conducted on the LAM-based TiAl alloys fabricated with different laser powers. The results are presented in Figure 9. The microhardness of the samples varies in the range of 475.1 to 534.8 HV, much higher than the corresponding as-cast counterparts reported in the literature, which are

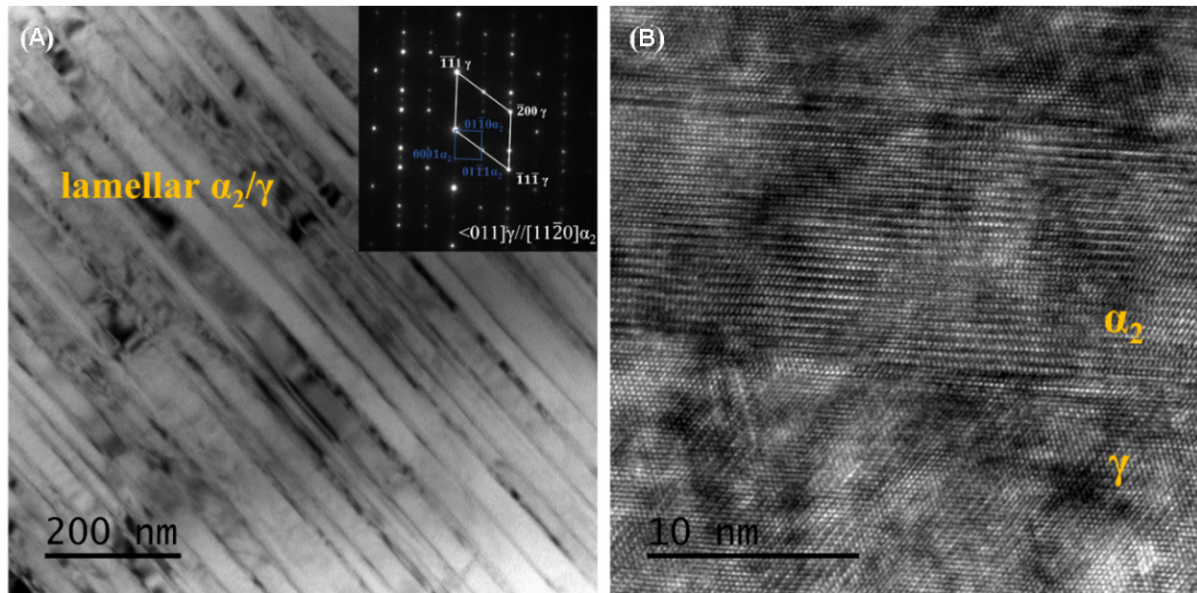


**Figure 5.** Structural details of lamellar colony characterized via TEM, showing an ultrafine lamellar structure. (A) TEM bright-field image showing the lamellae. The insert SADP showing the Blackburn orientation relationship followed by  $\alpha_2/\gamma$  lamellae. (B) HRTEM image presenting  $\alpha_2$  and  $\gamma$  plates.

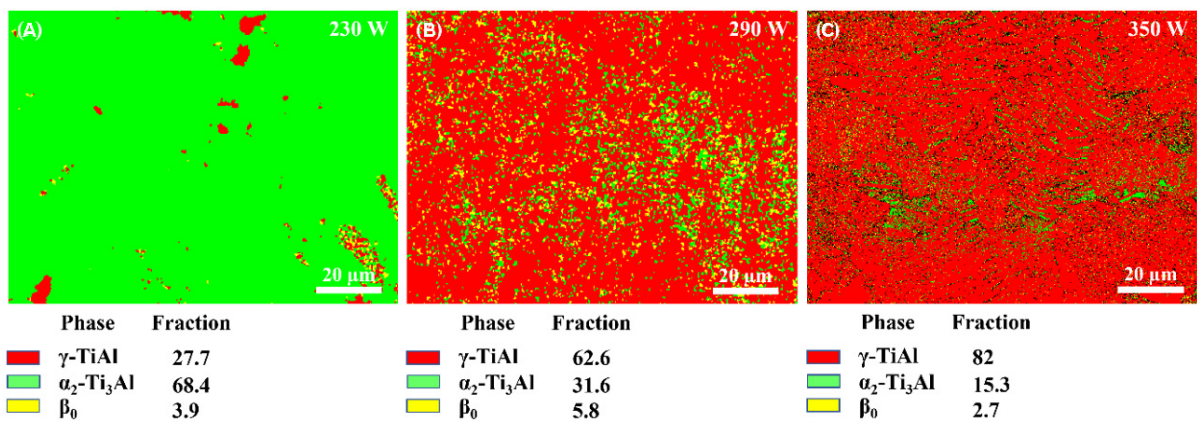


**Figure 6.** Phase maps from EBSD analysis showing the phase distribution and phase fraction of typical as-printed TiAl alloys fabricated by different laser powers: (A) 230; (B) 290; (C) 350 W. Red, green and yellow represent the  $\gamma$ ,  $\alpha_2$  and  $\beta_0$  phases, respectively. EBSD: Electron backscattered diffraction.

generally less than 351 HV<sup>[34]</sup>. In addition, it is evident that the microhardness is reduced with increasing laser power from 230 to 380 W. The reduction of the microhardness is mainly attributed to the following two reasons. At lower laser power, the phase composition is dominated by the  $\alpha_2$  phase. The  $\alpha_2$  phase was found to be harder than the  $\gamma$  phase and lamellar colony<sup>[4]</sup>. Therefore, the reduction in the  $\alpha_2$  phase decreases the microhardness. Furthermore, according to the Hall-Petch relation equation, the hardness of a material is dependent on its grain size. Thus, the hardness-grain size relation is described as<sup>[48]</sup>:

$$H = H_0 + K_H d^{-1/2} \tag{3}$$

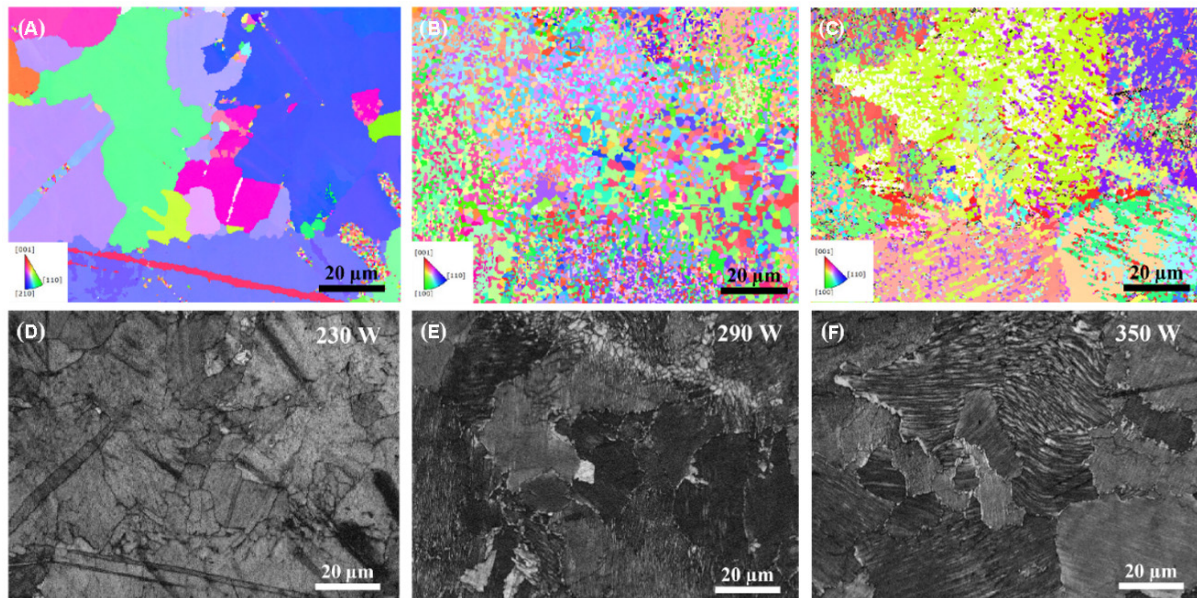


**Figure 7.** EBSD inverse pole figure maps and image quality maps showing grain orientation and distribution of as-printed TiAl alloys fabricated by different laser powers of (A) and (D) 230, (B) and (E) 290 and (C) and (F) 350 W. EBSD: Electron backscattered diffraction.

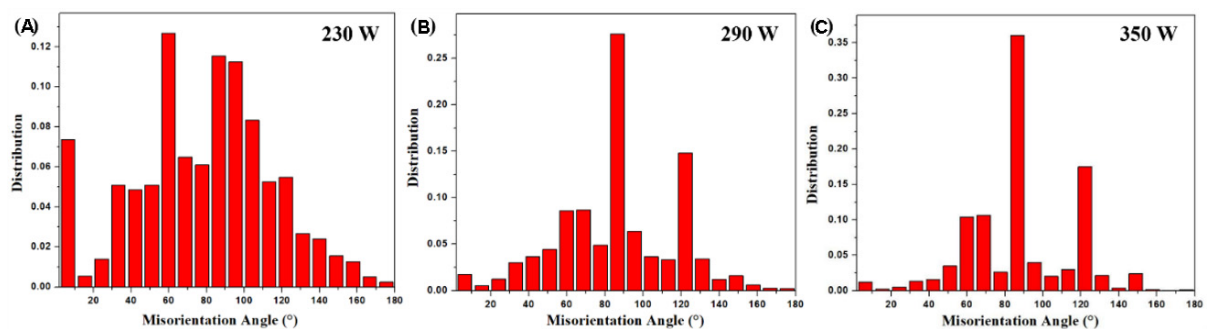


**Figure 8.** Grain orientation maps of as-printed TiAl samples fabricated by different laser powers of (A) 230, (B) 290 and (C) 350 W.

where  $H_0$  and  $K_H$  are constants. As discussed above, the grain size generally increases with increasing laser power, thus leading to the reduction in microhardness. In addition, due to the rapid cooling rate during the printing process, the LAM-based specimens exhibited refined grain size than the casting counterparts, contributing to the increase of microhardness in the as-printed state.

## CONCLUSION

In this study, a  $\beta$ -solidifying TiAl alloy, Ti-44Al-4Nb-1Mo-1Cr, was fabricated by LAM with different laser powers. Due to the complex thermal history during the LAM process, the as-printed intermetallic TiAl alloy samples showed susceptibility to cracking. Our work proved that the cracking problem could be mitigated by increasing the incident laser power to control the cooling rate. Nevertheless, the optimized process parameters could not suppress it totally. Therefore, future work is necessary to explore effective methods to achieve crack-free specimens. Several methods are worthy of investigation. For example, the optimized processing parameters combined with an external heating source can slow down the cooling rate and prevent cracking, or incorporation with hot isostatic pressing is possible to heal short cracks. Moreover, in

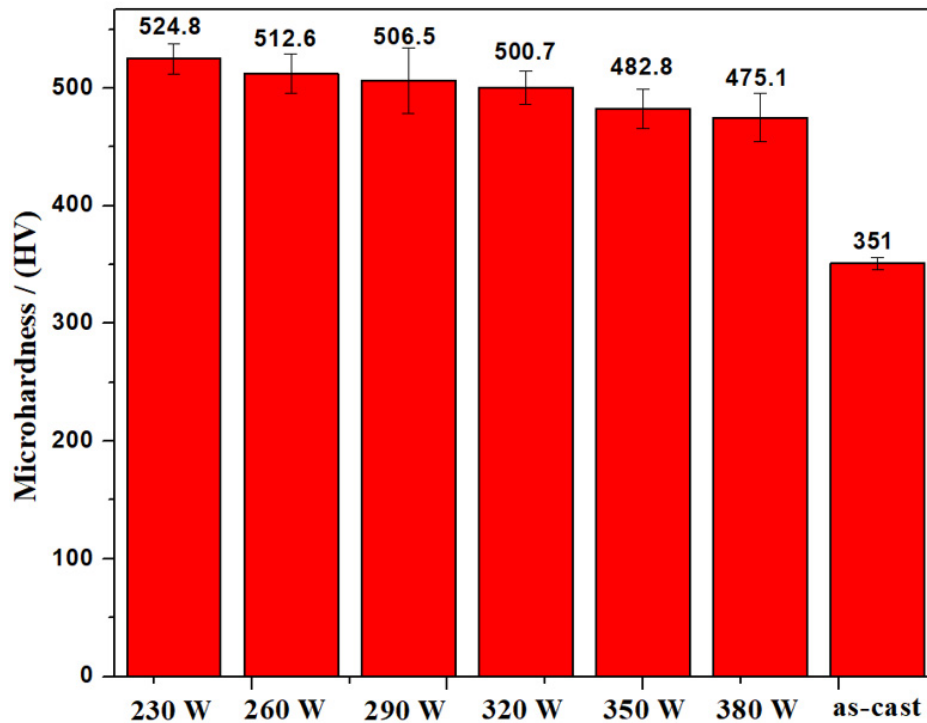


**Figure 9.** Microhardness of as-printed samples fabricated by different laser powers in comparison with the as-cast counterparts.

the present study, the operation parameter (laser power) has a significant effect on the microstructural evolution of the as-printed samples. The microstructure is dominated by brittle  $\alpha_2$  phase with lower laser power, while the microstructure exhibits a near-lamellar structure with an ultrafine lamellar spacing as the laser power increases to 380 W. The as-printed specimens all exhibited higher microhardness compared with that fabricated by casting.

## DECLARATIONS

### Acknowledgments

The authors would like to acknowledge the technical assistance of SUSTech Core Research Facilities.

### Authors' contributions

Contributed to conception and design of the study, data collection and analysis, manuscript drafting: Huang D

Contributed to the material characterization: Dong Y

Helped with material preparation: Chen H

Contributed to mechanism explanation: Zhou Y

Supervised the overall project: Zhang MX

Supervised the overall project: Yan M

### Availability of data and materials

Not applicable.

### Financial support and sponsorship

This study is supported by Research and Development Program Project in Key Areas of Guangdong Province (Grants No. 2019B090907001 and 2019B010943001), Natural Science Foundation of Guangdong

Province (2020A1515011373), the Central Guidance on Local: Construction of regional innovation system - Cross Regional R & D cooperation projects (20221ZDH04054) and ARC DP program (DP210103162).

### Conflicts of interest

All authors declared that there are no conflicts of interest.

### Ethical approval and consent to participate

Not applicable.

### Consent for publication

Not applicable.

### Copyright

© The Author(s) 2022.

## REFERENCES

1. Perrut M, Caron P, Thomas M, Couret A. High temperature materials for aerospace applications: Ni-based superalloys and  $\gamma$ -TiAl alloys. *Comptes Rendus Physique* 2018;19:657-71. DOI
2. Dimiduk DM. Gamma titanium aluminide alloys-an assessment within the competition of aerospace structural materials. *Mater Sci Eng* 1999;263:281-8. DOI
3. Wu X. Review of alloy and process development of TiAl alloys. *Intermetallics* 2006;14:1114-22. DOI
4. Niu HZ, Chen YY, Xiao SL, Xu LJ. Microstructure evolution and mechanical properties of a novel beta  $\gamma$ -TiAl alloy. *Intermetallics* 2012;31:225-31. DOI
5. Clemens H, Mayer S. Design, processing, microstructure, properties, and applications of advanced intermetallic TiAl alloys. *Adv Eng Mater* 2013;15:191-215. DOI
6. Kartavykh A, Asnis E, Piskun N, Statkevich I, Gorshenkov M, Korotitskiy A. A promising microstructure/deformability adjustment of  $\beta$ -stabilized  $\gamma$ -TiAl intermetallics. *Mater Lett* 2016;162:180-4. DOI
7. Clemens H, Wallgram W, Kremmer S, Güther V, Otto A, Bartels A. Design of novel  $\beta$ -solidifying TiAl alloys with adjustable  $\beta$ /B2-phase fraction and excellent hot-workability. *Adv Eng Mater* 2008;10:707-13. DOI
8. Mayer S, Erdely P, Fischer FD, et al. Intermetallic  $\beta$ -solidifying  $\gamma$ -TiAl based alloys - from fundamental research to application: intermetallic  $\beta$ -solidifying  $\gamma$ -TiAl based alloys. *Adv Eng Mater* 2017;19:1600735. DOI
9. Kothari K, Radhakrishnan R, Wereley NM. Advances in gamma titanium aluminides and their manufacturing techniques. *Prog Aerosp Sci* 2012;55:1-16. DOI
10. Thomas M, Raviart JL, Popoff F. Cast and PM processing development in gamma aluminides. *Intermetallics* 2005;13:944-51. DOI
11. Sahasrabudhe H, Bose S, Bandyopadhyay A. Laser-based additive manufacturing processes. *Adva Laser Mater Proc* 2018:507-39. DOI
12. Li S, Li J, Jiang Z, et al. Controlling the columnar-to-equiaxed transition during directed energy deposition of inconel 625. *Addit Manufact* 2022;57:102958. DOI
13. Narayana P, Li C, Kim S, et al. High strength and ductility of electron beam melted  $\beta$  stabilized  $\gamma$ -TiAl alloy at 800 °C. *Mater Sci Eng* 2019;756:41-5. DOI
14. Wartbichler R, Clemens H, Mayer S. Electron beam melting of a  $\beta$ -solidifying intermetallic titanium aluminide alloy. *Adv Eng Mater* 2019;21:1900800. DOI
15. Baudana G, Biaino S, Klöden B, et al. Electron beam melting of Ti-48Al-2Nb-0.7Cr-0.3Si: feasibility investigation. *Intermetallics* 2016;73:43-9. DOI
16. Lin B, Chen W, Yang Y, Wu F, Li Z. Anisotropy of microstructure and tensile properties of Ti-48Al-2Cr-2Nb fabricated by electron beam melting. *J Alloys Compd* 2020;830:154684. DOI
17. Schwerdtfeger J, Körner C. Selective electron beam melting of Ti-48Al-2Nb-2Cr: microstructure and aluminium loss. *Intermetallics* 2014;49:29-35. DOI
18. Bhavar PKV, Patil V, Khot S, Gujar K, Singh R. A review on powder bed fusion technology of metal additive manufacturing, In 4th international conference and exhibition on additive manufacturing technologies-AM-2014, 1-2 September 2014, Bangalore, India. DOI
19. Sharman A, Hughes J, Ridgway K. Characterisation of titanium aluminide components manufactured by laser metal deposition. *Intermetallics* 2018;93:89-92. DOI
20. Yan Z, Liu W, Tang Z, et al. Review on thermal analysis in laser-based additive manufacturing. *Opt Laser Technol* 2018;106:427-41. DOI
21. Zheng B, Zhou Y, Smugeresky J, Schoenung J, Lavernia E. Thermal behavior and microstructural evolution during laser deposition

- with laser-engineered net shaping: part I. numerical calculations. *Metall Mat Trans A* 2008;39:2228-36. DOI
22. Srivastava D, Chang ITH, Loretto MH. The effect of process parameters and heat treatment on the microstructure of direct laser fabricated TiAl alloy samples. *Intermetallics* 2001;9:1003-13. DOI
  23. Balla VK, Das M, Mohammad A, Al-ahmari AM. Additive manufacturing of  $\gamma$ -TiAl: processing, microstructure, and properties: additive manufacturing of  $\gamma$ -TiAl: processing. *Adv Eng Mater* 2016;18:1208-15. DOI
  24. Li W, Liu J, Zhou Y, et al. Effect of laser scanning speed on a Ti-45Al-2Cr-5Nb alloy processed by selective laser melting: microstructure, phase and mechanical properties. *J Alloys Compd* 2016;688:626-36. DOI
  25. Löber L, Schimansky FP, Kühn U, Pyczak F, Eckert J. Selective laser melting of a beta-solidifying TNM-B1 titanium aluminide alloy. *J Mater Proc Technol* 2014;214:1852-60. DOI
  26. Biamino S, Penna A, Ackelid U, et al. Electron beam melting of Ti-48Al-2Cr-2Nb alloy: microstructure and mechanical properties investigation. *Intermetallics* 2011;19:776-81. DOI
  27. Huang SH, Liu P, Mokasdar A, Hou L. Additive manufacturing and its societal impact: a literature review. *Int J Adv Manuf Technol* 2013;67:1191-203. DOI
  28. Zhou Y, Li W, Wang D, et al. Selective laser melting enabled additive manufacturing of Ti-22Al-25Nb intermetallic: excellent combination of strength and ductility, and unique microstructural features associated. *Acta Mater* 2019;173:117-29. DOI
  29. Brion DA, Shen M, Pattinson SW. Automated recognition and correction of warp deformation in extrusion additive manufacturing. *Addit Manuf* 2022;56:102838. DOI
  30. Abdulrahman KO, Akinlabi ET, Mahamood RM. Characteristics of laser metal deposited titanium aluminide. *Mater Res Express* 2019;6:046504. DOI
  31. Liu W, Dupont JN. Fabrication of carbide-particle-reinforced titanium aluminide-matrix composites by laser-engineered net shaping. *Metall Mater Trans A* 2004;35:1133-40. DOI
  32. Li W, Liu J, Wen S, Wei Q, Yan C, Shi Y. Crystal orientation, crystallographic texture and phase evolution in the Ti-45Al-2Cr-5Nb alloy processed by selective laser melting. *Mater Charact* 2016;113:125-33. DOI
  33. Xu H, Li X, Xing W, Shu L, Ma Y, Liu K. Solidification pathway and phase transformation behavior in a beta-solidified gamma-TiAl based alloy. *J Mater Sci Technol* 2019;35:2652-7. DOI
  34. Schwaighofer E, Clemens H, Mayer S, et al. Microstructural design and mechanical properties of a cast and heat-treated intermetallic multi-phase  $\gamma$ -TiAl based alloy. *Intermetallics* 2014;44:128-40. DOI
  35. Ramanujan R. Phase transformations in  $\gamma$  based titanium aluminides. *Int Mater Rev* 2000;45:217-40. DOI
  36. Yang G, Ren W, Liu Y, et al. Effect of pre-deformation in the  $\beta$  phase field on the microstructure and texture of the  $\alpha$  phase in a boron-added  $\beta$ -solidifying TiAl alloy. *J Alloys Compd* 2018;742:304-11. DOI
  37. Hu D, Huang A, Wu X. On the massive phase transformation regime in TiAl alloys: the alloying effect on massive/lamellar competition. *Intermetallics* 2007;15:327-32. DOI
  38. Sankaran A, Bouzy E, Humbert M, Hazotte A. Variant selection during nucleation and growth of  $\gamma$ -massive phase in TiAl-based intermetallic alloys. *Acta Materialia* 2009;57:1230-42. DOI
  39. Sun YQ. Surface relief and the displacive transformation to the lamellar microstructure in TiAl. *Philosophy Magaz Lett* 1998;78:297-305. DOI
  40. Chaturvedi M, Xu Q, Richards N. Development of crack-free welds in a TiAl-based alloy. *J Mater Proc Technol* 2001;118:74-8. DOI
  41. Srivastava D, Chang I, Loretto M. The optimisation of processing parameters and characterisation of microstructure of direct laser fabricated TiAl alloy components. *Mater Design* 2000;21:425-33. DOI
  42. Denquin A, Naka S. Phase transformation mechanisms involved in two-phase TiAl-based alloys-I. lamellar structure formation. *Acta Materialia* 1996;44:343-52. DOI
  43. Kasthuber M, Rashkova B, Clemens H, Mayer S. Enhancement of creep properties and microstructural stability of intermetallic  $\beta$ -solidifying  $\gamma$ -TiAl based alloys. *Intermetallics* 2015;63:19-26. DOI
  44. Bernal D, Chamorro X, Hurtado I, Madariaga I. Evolution of lamellar microstructures in a cast TNM alloy modified with boron through single-step heat treatments. *Intermetallics* 2020;124:106842. DOI
  45. Song B, Dong S, Zhang B, Liao H, Coddet C. Effects of processing parameters on microstructure and mechanical property of selective laser melted Ti6Al4V. *Mater Design* 2012;35:120-5. DOI
  46. Berteaux O, Popoff F, Thomas M. An experimental assessment of the effects of heat treatment on the microstructure of Ti-47Al-2Cr-2Nb powder compacts. *Metall Mat Trans A* 2008;39:2281-96. DOI
  47. Li M, Wu X, Yang Y, et al. TiAl/RGO (reduced graphene oxide) bulk composites with refined microstructure and enhanced nanohardness fabricated by selective laser melting (SLM). *Mater Charact* 2018;143:197-205. DOI
  48. Taha AS, Hammad FH. Application of the hall-petch relation to microhardness measurements on Al, Cu, Al-MD 105, and Al-Cu alloys. *Physica Status Solidi* 1990;119:455-62. DOI